# A Transient and Low-Populated Protein-Folding Intermediate at Atomic Resolution

Dmitry M. Korzhnev,[1] Tomasz L. Religa,[1] Wiktor Banachewicz,[2] Alan R. Fersht,[2] Lewis E. Kay[1]*

Proteins can sample conformational states that are critical for function but are seldom detected directly because of their low occupancies and short lifetimes. In this work, we used chemical shifts and bond-vector orientation constraints obtained from nuclear magnetic resonance relaxation dispersion spectroscopy, in concert with a chemical shift–based method for structure elucidation, to determine an atomic-resolution structure of an "invisible" folding intermediate of a small protein module: the FF domain. The structure reveals non-native elements preventing formation of the native conformation in the carboxyl-terminal part of the protein. This is consistent with the kinetics of folding in which a well-structured intermediate forms rapidly and then rearranges slowly to the native state. The approach introduces a general strategy for structure determination of low-populated and transiently formed protein states.

There is increasing evidence that metastable intermediates are ubiquitous along protein-folding pathways (*1*–*7*). Because they are transiently formed and weakly populated, the detection and characterization of these excited states remains a challenge. Recent developments in relaxation dispersion nuclear magnetic resonance (NMR) spectroscopy provide an opportunity for detailed study of such rare states (*5*, *8*, *9*). Although they cannot be detected in NMR spectra, the presence of these "invisible" conformers nevertheless leads to broadening of peaks derived from nuclei within the "visible" ground-state structure. Such excess line broadening can be quantified, providing that conformers in the ground state exchange with those in the excited state on the millisecond timescale with fractional excited-state populations of at least 0.5% (*10*). In this case, by recording the decay rate of transverse magnetization $R_{2,\mathrm{eff}}$ (Fig. 1A) as a function of the strength of an applied radio-frequency field ($\nu_{\mathrm{CPMG}}$), it is possible to extract the kinetics and thermodynamics of the exchange process, as well as the chemical shifts of the $^{1}$H, $^{13}$C, or $^{15}$N probed nuclei (*8*, *11*). In a related class of experiments recorded under conditions of weak molecular alignment, residual dipolar couplings (RDCs) that report on the relative orientation of bond vectors in the excited state can be measured (*12*, *13*).

Previously, our laboratory has inferred structural properties of low-populated folding intermediates by comparing limited numbers of NMR chemical shifts of the intermediate with the corresponding shifts that are predicted for an unfolded, random coil ensemble (*5*, *14*, *15*). However, obtaining an extensive set of chemical shifts and bond-vector orientations (*8*, *9*) opens the possibility of calculating detailed three-dimensional (3D) atomic-resolution models of invisible excited states (*16*). Central to the structure calculations is the emergence of robust computational protocols that do not rely on experimental distance restraints, but instead employ backbone chemical shifts in concert with structural databases (*17*–*19*). Accurate structures for ground states of small proteins on the order of 120 residues or less are obtained in this manner. We have used backbone $^{15}$N, $^{1}$H$^{N}$, $^{13}$C$^{\alpha}$, $^{1}$H$^{\alpha}$, and $^{13}$C$^{O}$ chemical shifts, as well as amide bond-vector orientations, to generate a structure of an invisible folding intermediate of the wild-type (WT) FF domain from HYPA/FBP11 (*20*) with an equilibrium population of 2 to 3% and a millisecond lifetime.

**Relaxation dispersion measurements.** The FF domain from HYPA/FBP11 is a small 71-residue, four-helix bundle with H1(α)-H2(α)-H3($3_{10}$)-H4(α) topology (*20*) that folds by a three-state mechanism involving an on-pathway intermediate (I): U ↔ I ↔ N (*14*, *21*–*23*). Folding proceeds in two phases, including the fast formation of I from the unfolded state U (microsecond time scale) and a slower, rate-limiting transition from I to the native state.

[1]Departments of Molecular Genetics, Biochemistry, and Chemistry, the University of Toronto, Toronto, Ontario M5S 1A8, Canada. [2]Medical Research Council Centre for Protein Engineering, Hills Road, Cambridge CB2 2QH, UK.

*To whom correspondence should be addressed. E-mail: kay@pound.med.utoronto.ca

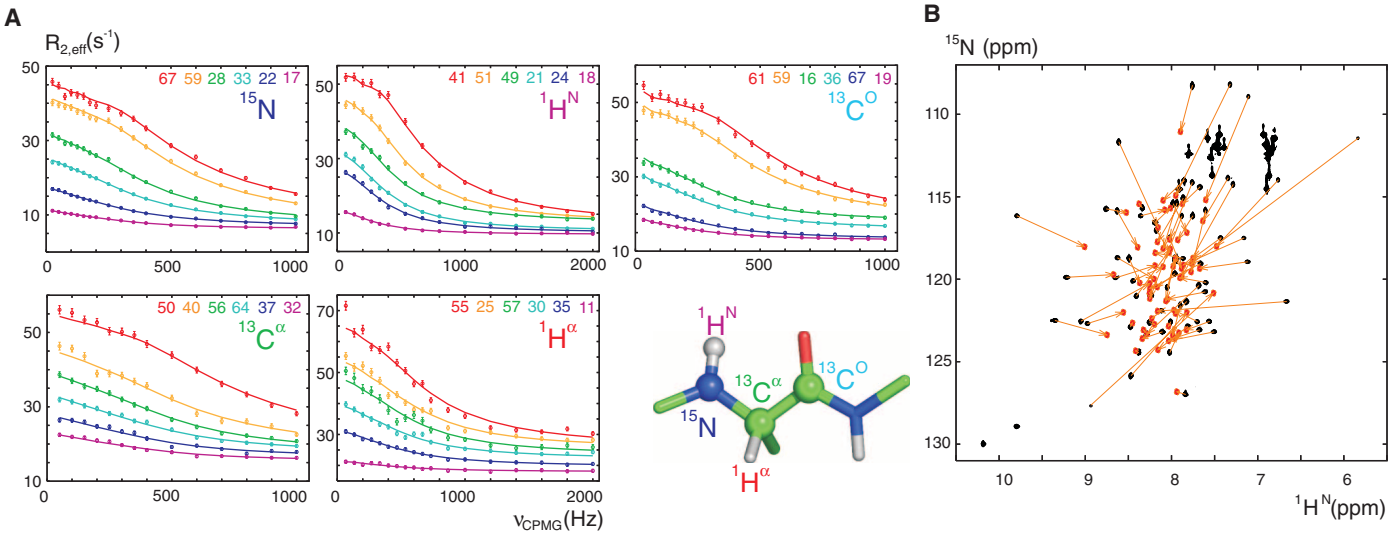


**Fig. 1.** Probing the invisible intermediate state by relaxation dispersion NMR. (**A**) Experimental relaxation dispersion profiles for select backbone $^{15}$N (*12*, *26*), $^{1}$H$^{N}$ (*27*), $^{13}$C$^{\alpha}$ (*11*), $^{1}$H$^{\alpha}$ (*29*), and $^{13}$C$^{O}$ (*11*, *30*) nuclei of the WT FF domain ($FF_{1\text{-}71}$) measured at a static magnetic field of 18.8 T (open circles), along with best fits to a two-site exchange model, I ↔ N, performed as described elsewhere (solid lines) (*5*). Residue numbers are shown in the top right corner of each box. Error bars indicate uncertainties in $R_{2,\mathrm{eff}}$ rates. The experiments made use of protein samples with specifically tailored isotope labeling schemes [U-$^{15}$N,$^{13}$C,$^{2}$H-labeling for $^{15}$N, $^{1}$H$^{N}$, $^{13}$C$^{O}$ dispersion experiments, 30°C; selective-$^{13}$C$^{\alpha}$ labeling, full protonation (*49*) for $^{13}$C$^{\alpha}$ experiments, 30°C; U-$^{15}$N,$^{13}$C, ≈50%-$^{2}$H labeling (*29*) for $^{1}$H$^{\alpha}$ experiments, 35°C], and the data were analyzed separately for each type of nucleus as described in (*32*). The extracted values of $\Delta\varpi_{\mathrm{IN}}$, with signs of chemical-shift differences determined as described previously (*33*, *50*), are used for calculating the chemical shifts of the invisible intermediate, $\varpi_{\mathrm{I}} = \varpi_{\mathrm{N}} + \Delta\varpi_{\mathrm{IN}}$, allowing reconstruction of its NMR spectra. The reconstructed $^{15}$N,$^{1}$H$^{N}$ correlation map of the I state (orange) and the experimental spectrum of the N state (black) are shown in (**B**). ppm, chemical shifts in parts per million.

tively folded state N (millisecond time scale) (*21*). The transition state between I and N has been characterized previously by Φ-value analysis (*24*) with 50 mutations, establishing that this state contains a structured core centered at the end of H1 and the beginning of H2 (*22*).

We performed a series of NMR relaxation dispersion experiments focusing on $^{15}N$, $^{1}H^{N}$, $^{13}C^{\alpha}$, $^{1}H^{\alpha}$, and $^{13}C^{O}$ nuclei of the protein backbone (Fig. 1A) (*11*, *12*, *25*–*30*). In a previous study of the folding of $Ala^{17} \rightarrow Gly^{17}$ (A17G) and Q19G (*31*) mutant FF domains, $^{15}N$ relaxation dispersion data could only be properly fit with the use of a model of three-site exchange with an on-pathway intermediate (*14*). However, for the WT domain, the U ↔ I transition could not be detected due to the extremely fast rate of interconversion between these states (*21*) and the low population of U relative to I [$p_U/p_I < 0.2$, based on hydrogen-deuterium exchange data (*14*), where $p_U$ and $p_I$ are fractional populations of states U and I, respectively]. Consistent with this finding, the dispersion data in this study were well fit, assuming a model of two-state exchange, $I \underset{k_{N\rightarrow I}}{\overset{k_{I\rightarrow N}}{\rightleftharpoons}} N$, where $k_{I\rightarrow N}$ and $k_{N\rightarrow I}$ are rate constants [see the supporting online material (SOM)] (*32*). This allowed extraction of the population $p_I$, the exchange rate constant $k_{ex} = k_{N\rightarrow I} + k_{I\rightarrow N}$, and absolute values of chemical-shift differences between states $|\Delta\varpi_{IN}|$. From $|\Delta\varpi_{IN}|$, the chemical shifts $\varpi_I = \varpi_N + \Delta\varpi_{IN}$ were subsequently obtained (*33*) for more than 90% of the possible backbone resonances in the protein. We performed $^{15}N$ experiments at 30°C using a uniformly $^{15}N$,$^{13}C$,$^{2}H$-labeled sample in $H_2O$ buffer, which gave $p_I = 2.84 \pm 0.02\%$ and $k_{ex} = 1817 \pm 14\ s^{-1}$, with some variation in $p_I$ and $k_{ex}$ for samples dissolved in $^{2}H_2O$ ($^{1}H^{\alpha}$ dispersion experiments) or fully protonated ($^{13}C^{\alpha}$ experiments). Figure 1B compares $^{15}N$,$^{1}H^{N}$ spectra of the visible N state (black) with the reconstructed data set of the invisible intermediate (orange) on the basis of chemical shifts extracted from fits of the dispersion data.

We obtained backbone $^{1}H^{N}$-$^{15}N$ RDCs (92% of residues) by recording dispersion experiments under conditions of fractional protein alignment (*12*, *34*). Together, the backbone chemical shifts and amide RDCs constitute the experimental data that we used to calculate structures of the WT FF folding intermediate.

**Secondary structure and flexibility of the intermediate state from chemical shifts.** Chemical shifts are very sensitive probes of local protein conformation from which protein secondary structure can be determined (*35*). They also report on protein flexibility that can be empirically estimated by the random coil index (RCI) method (*36*). We have used $\varpi_I$ values to initially assess secondary structure and dynamics of the folding intermediate.

The secondary structures of the N and I states of the FF domain predicted from backbone chemical shifts using the TALOS+ program (*37*) are highlighted in Fig. 2A, superimposed on the tertiary folds of these states that were generated by standard NMR methods [N state (*20*)] or by using the approach detailed below (I state). Not surprisingly, TALOS+ correctly identifies the four helices, H1 to H4, of the native state. The intermediate also comprises four helices, and H1 and H2 have similar boundaries to those observed in the native state. However, the third helix of the intermediate is non-native, spanning residues $Arg^{48}$ (R48) to L55 (*31*) that form the $3_{10}$-helix H3, the H3-H4 loop, and the beginning of H4 in the native protein. The fourth (and C-terminal) helix in the intermediate, extending from K59 to K66, is not as well defined as the other helices.

Squared order parameters ($S^2$), measuring amplitudes of motion for the backbone amide groups, obtained by the RCI approach (*36*) clearly suggest that the intermediate state has a well-structured core of ~45 residues that includes helices H1 to H3, flanked by more flexible N- and C-termini (Fig. 2B). Notably, the predicted order parameters for helices H1 to H3 are similar in the I and N states, with $S^2$ values between 0.7 to 0.9 for the intermediate, although the loop between H1 and H2 and the C terminus of H3 are more dynamic. Finally, $S^2$ values of ≈0.6 are obtained for residues in helix H4 of the intermediate, suggesting that this element is less stably formed in the I state, which is consistent with previously reported hydrogen-deuterium exchange data (*14*).

**Structure determination of the folding intermediate by CS-Rosetta.** Recently, substantial progress has been achieved in the development of computational approaches for de novo protein structure determination in which short protein fragments that are compatible with experimental chemical shifts are selected from a structural database and subsequently assembled into 3D models (*17*–*19*). Structures of proteins smaller than ~120 residues calculated in this manner have an accuracy better than 2 Å. The methodology can be further extended to larger proteins in cases where small numbers of backbone distance restraints can be measured (*38*); unfortunately, this is not possible presently in studies of invisible excited states. In this work, we have made use of one such chemical shift–based method for structure determination, CS-Rosetta (*18*, *39*). We have modified the scoring function during the final structure-selection stage to include residuals between predicted and measured RDC values in addition to the Rosetta energy that has been rescored to include experimental chemical shifts, as described previously (*18*) (see SOM materials and methods). The protocol was first tested using backbone $^{1}H$, $^{13}C$, and $^{15}N$ chemical shifts of the native WT FF domain, $\varpi_N$. An accurate model of the native state was generated with a 1.4 Å backbone root-mean-squared deviation (RMSD) to the experimentally determined NMR structure (*20*) and with correctly packed side chains (fig. S1).

We performed calculations of structures of the I state for residues 11 to 66 that exclude flexible N- and C-termini that may adversely affect the convergence of the CS-Rosetta protocol (*18*). Figure 3A shows the typical funnel-like shape of the CS-Rosetta energy function versus RMSD to the lowest-energy structure that is characteristic of converged structure calculations. The structures produced are well defined with a mean pairwise backbone RMSD among the 10 lowest-energy structures of 1.1 Å calculated for residues with $S^2 > 0.7$ (see SOM materials and methods). Although RDC values have been included in the final scoring function for "rigid" residues, very similar structures are obtained, irrespective of whether such restraints are used. The mean RMSD between backbone-heavy atoms of structures calculated with and without RDC values is 1.25 Å for residues with $S^2 > 0.7$, and the lowest-energy conformers in each set of structures are identical.

Calculated intermediate-state structures are in excellent agreement with the input experimental data. For example, the overall lowest-energy model of the intermediate state is in the top 3, 0.2, and 0.2% of all structures based on Rosetta, chemical-shift, and RDC energies, respectively. Figure 3, B

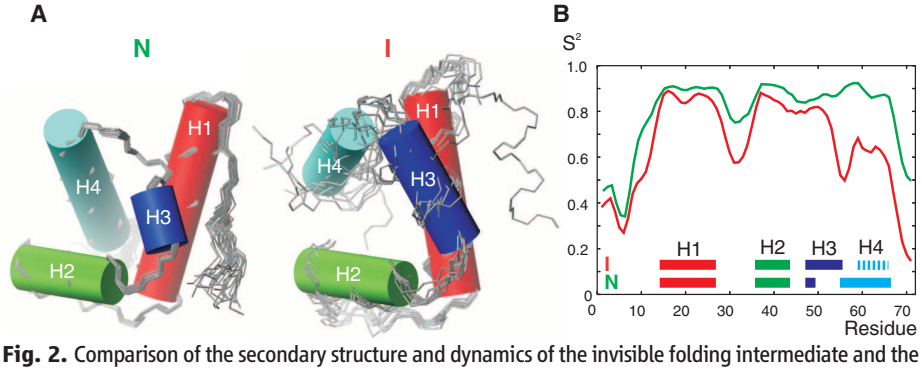


**Fig. 2.** Comparison of the secondary structure and dynamics of the invisible folding intermediate and the native state of the WT FF domain. (**A**) Helix boundaries are as predicted by TALOS+ (*37*) based on a nearly complete set of backbone chemical shifts: 14 to 27, 36 to 43, 48 to 49, and 54 to 67 in the native state and 14 to 27, 36 to 43, 48 to 55, and 59 to 66 in the intermediate. The helices are depicted by rods superimposed onto an ensemble of the NMR-derived structures of the native state (N) [PDB accession code 1UZC (*20*)] or onto an ensemble of 10 representative structures of the intermediate (I), calculated by CS-Rosetta (*18*). (**B**) $S^2$ values for the backbone amide groups of the folding intermediate (red) and native state (green), as predicted by the RCI approach (*36*).

and C, show that a high level of agreement is obtained between experimental chemical shifts and RDC constraints and the corresponding values generated by averaging over shifts and RDCs predicted from each of the 10 lowest-energy structures. The excellent correlation between experimental and calculated chemical shifts provides a measure of confidence in the calculated secondary structure and, to some extent, tertiary interactions, whereas the agreement between measured and predicted RDCs for residues in H1 to H3 indicates that the relative orientation of these helices is correctly captured. In contrast, measured and calculated RDC values for H4 agree much less well with each other, consistent with the fact that this helix is dynamic and only partially formed. RDC values in the intermediate state span a range of more than 100 Hz, several times larger than for the native state. This indicates that the intermediate interacts more extensively than the native state with the polyethylene glycol/hexanol medium (*40*) used for protein alignment, perhaps due to the disordered H4 that would have greater accessibility to the alignment medium.

**Structure of the intermediate reveals details of the folding pathway.** Figure 4 compares the lowest-energy intermediate and native-state structures. As predicted from $S^2$ parameters, the intermediate has a well-defined core of ~45 residues that includes α helices H1 to H3. The poorly defined helix H4 has a preferential orientation similar to that of the native H4. The orientations and lengths of helices H1, H2, and the intervening loop are also similar in both states. As predicted by TALOS+, α helix H3 is non-native, including residues that make up helix H3, the H3-H4 loop, and the beginning of α helix H4 in the native structure. Thus, it is not possible for a nativelike H4 to form. The longer H3 docks against H1, and the H1-H3 interface in the intermediate state comprising residues A17, A20, L24 of H1, and L52, L55 of H3 forms interactions distinct from those in the native protein. Additional non-native interactions in the intermediate state are observed at the interface of α helices H2 and H3 involving a hydrophobic cluster consisting of A53, Y49, and I44.

Thus, a substantial number of non-native interactions must be broken before formation of the native conformation, which is probably the reason why the I-to-N transition is rate-limiting for FF domain folding. The model for the intermediate state produced here also provides a structural basis for understanding results from a previous Φ-value analysis of the rate-limiting transition state (*22*). That study concluded that secondary and tertiary interactions are fully formed (large Φ values) only in a relatively small region of the protein including the end of α helix H1, the H1-H2 loop, and the beginning of helix H2. This is the part of the FF domain that is structurally conserved between the I and N states. In contrast, low Φ values were observed for both A17G and A20G mutations in the beginning of H1 and for A51G and L52A in the H3-H4 loop of the native state that is part of helix H3 in the intermediate. The structures of I and N, together with the previous Φ-value analysis (*22*), establish that non-native contacts formed by these residues must be broken between the intermediate state and the rate-limiting transition state along the folding pathway.

**A mimic of the intermediate by selective destabilization of the native state.** The primary difference between the I and N states of the FF domain is the non-native α helix H3 that prevents formation of the native C-terminal helix H4 that, in turn, is essential for stabilizing the native structure (*20*, *22*). For example, the F62A mutation leads to a completely destabilized domain (*22*). Low $^1H/^2H$-exchange protection factors for the backbone amide groups (*14*) and enhanced flexibility predicted by the RCI approach (Fig. 2) (*36*) suggest that the C-terminal region of the FF domain is at least partially disordered in the intermediate and, therefore, probably only marginally affects the stability of the I state. This suggests that a strategy for selective destabilization of the native state and isolation of a mimic of the folding intermediate might be to cut off the C-terminal part of the protein that includes the native α helix H4.

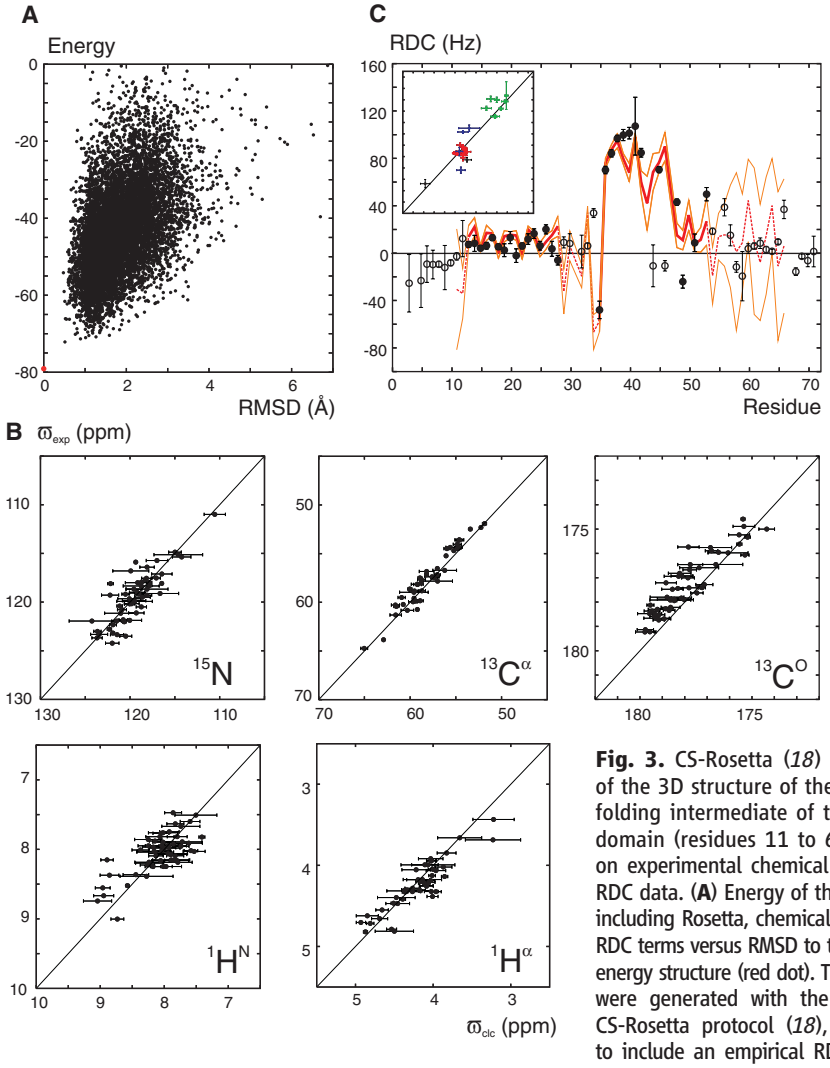


**Fig. 3.** CS-Rosetta (*18*) modeling of the 3D structure of the invisible folding intermediate of the WT FF domain (residues 11 to 66) based on experimental chemical shift and RDC data. (**A**) Energy of the models, including Rosetta, chemical-shift, and RDC terms versus RMSD to the lowest-energy structure (red dot). The models were generated with the standard CS-Rosetta protocol (*18*), modified to include an empirical RDC energy term at the final stage of re-scoring the calculated structural models. Ten thousand models of the intermediate were generated, of which the 10 with the lowest energies were analyzed. (**B**) Correlation plots of experimental $^{15}N$, $^{1}H^{N}$, $^{13}C^{\alpha}$, $^{1}H^{\alpha}$, and $^{13}C^{O}$ chemical shifts of the WT intermediate, $\varpi_{exp}$, versus chemical shifts predicted by the SPARTA program (*51*), $\varpi_{clc}$, averaged over an ensemble of the 10 lowest-energy models. The distributions of calculated chemical shifts in the ensemble (1 SD) are indicated by horizontal lines (error bars). (**C**) Plots of experimental (circles) and back-calculated (red lines) $^{1}H^{N}$-$^{15}N$ RDC values averaged over the 10 lowest-energy intermediate structures, as well as the standard deviation in predicted RDC values (orange lines). RDC data for residues with RCI $S^2 > 0.7$ used in scoring of the assembled models are shown by filled circles/solid lines, whereas measured RDC values for residues with $S^2 < 0.7$ or with large uncertainties are indicated by open circles. The dashed red line denotes the average over RDC values calculated for each structure of the ensemble for residues that were not restrained by dipolar couplings in the calculations. (Inset) Experimental RDC values for the core residues (helix H1, red; H2, green; H3, blue) plotted versus back-calculated values averaged over an ensemble of the 10 best structures. Errors in experimental RDC values are indicated by vertical bars, whereas the distributions in the calculated RDC values from the ensemble (1 SD) are indicated by horizontal lines.

With this in mind, we expressed and purified a variant WT FF domain that includes residues 1 to 60: $FF_{1-60}$ (referred to as I′). This truncated version displays a cooperative thermal-denaturation transition (*41*) with a melting temperature $T_m$ of 39.3 ± 2.8°C and a denaturation enthalpy $\Delta H_{U\text{-}I'}$ ($T_m$) = 14.2 ± 0.9 kcal/mol (Fig. 5A). The presence of a cooperative transition suggests that $FF_{1-60}$ is well folded and not a large collection of structurally heterogeneous molecules, consistent with expectations for a mimic of the intermediate state. Laser-induced temperature-jump experiments (*23*, *42*) from 22° to 25°C indicate that the truncated FF domain folds with a single kinetic phase $k_{U\rightarrow I'} \sim 10^5\ s^{-1}$ (Fig. 5B), which corresponds to the fast (microsecond–timescale) formation of the folding intermediate in the full-length domain (*21*, *23*).

Although prone to aggregation, the truncated FF domain is amenable to triple-resonance NMR studies that provide backbone $^1H$, $^{15}N$, and $^{13}C$ resonance assignments (*43*, *44*). Figure 5C shows the correlation of $^{15}N$, $^1H^N$, $^{13}C^\alpha$, $^1H^\alpha$, and $^{13}C^O$ chemical-shift differences between $FF_{1-60}$ and the native full-length domain $FF_{1-71}$ ($\Delta\varpi_{spec}$), with chemical-shift differences between intermediate and native states of $FF_{1-71}$ obtained from relaxation dispersion data ($\Delta\varpi_{disp}$). The chemical shifts of $FF_{1-60}$ and the transiently populated intermediate are quite similar, except for a few residues located proximal to the site of truncation. Therefore, the designed variant must have a structure nearly identical to that of the folding intermediate of the full-length WT FF domain. The quality of the nuclear Overhauser effect spectroscopy (NOESY) spectrum recorded for $FF_{1-60}$ does not permit a detailed structural characterization of this truncated domain. Whereas there are cross-peaks at $^1H$ methyl frequencies connecting A17 and A20 with L52(δ1 and δ2) and L55(δ1) that form the non-native interface between helices H1 and H3 in the intermediate state, potential overlap with other peaks prevents unambiguous NOE assignments in this region.

Although the folding intermediate of the WT FF domain from HYPA/FBP11 forms rapidly (on the microsecond–timescale), the 3D structural model of the I state shows that its rearrangement to the native conformation can only occur through the breaking of non-native secondary and tertiary interactions that slow the folding process by approximately two orders of magnitude. Non-native interactions along folding pathways that trap intermediate states may be more common than appreciated. The α-helical proteins Im7 (*4*), Rd-apocytb$_{562}$ (*45*), the R16 and R17 domains of α-spectrin (*46*), and EnHD (*47*) all fold via intermediates with non-native interactions that must be broken in a rate-limiting step before formation of native structures (*48*).

The methodology presented here for structural studies of invisible, transiently formed protein states is not restricted to folding intermediates but includes excited states important for function—for example, enzyme catalysis and ligand binding. As such, relaxation dispersion NMR spectroscopy holds great promise for providing important structural information on a large number of elusive conformers that play critical roles in a wide range of biochemical processes.

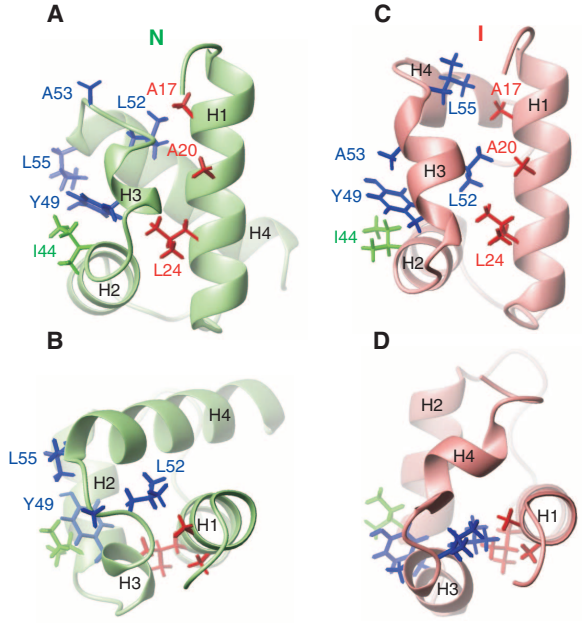


**Fig. 4.** Non-native interactions in the intermediate state. Structure and packing in the FF domain–folding intermediate [pink, (**C** and **D**)] as compared with the native protein [light green, (**A** and **B**); PDB code 1UZC (*20*)]. Side chains of residues from helices H1 (red), H2 (green), and H3 (blue) that form non-native contacts in the intermediate state are outlined. Structures on the bottom [(B) and (D)] are rotated by 90° relative to those on the top.

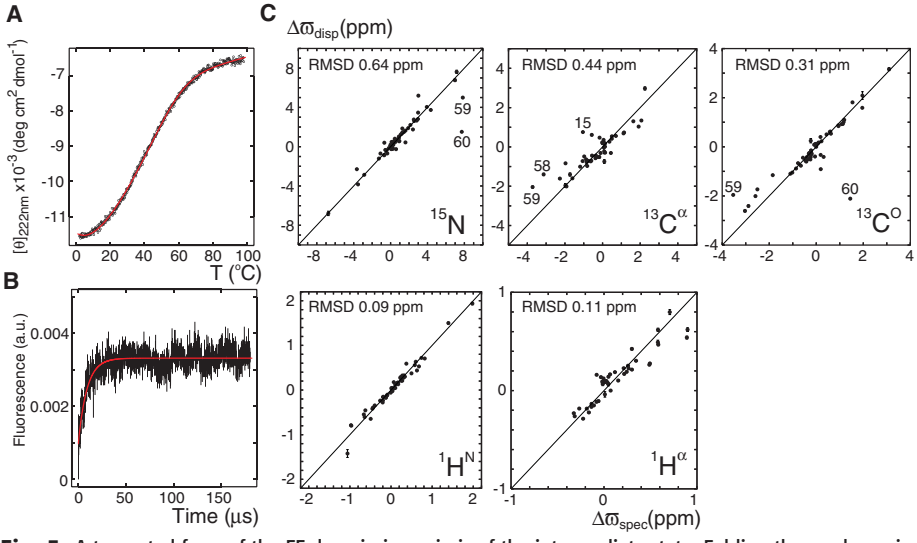


**Fig. 5.** A truncated form of the FF domain is a mimic of the intermediate state. Folding thermodynamics and kinetics of $FF_{1-60}$ are characterized, respectively, by (**A**) thermal denaturation monitored by far ultraviolet circular dichroism (*41*) and (**B**) a laser-induced temperature jump (from 23° to 25°C) monitored by fluorescence (*23*, *42*). θ, ellipticity; T, temperature; a.u., arbitrary units. The red lines indicate fits to the experimental data (black). (**C**) Backbone $^{15}N$, $^1H^N$, $^{13}C^\alpha$, $^1H^\alpha$, and $^{13}C^O$ chemical-shift differences between $FF_{1-60}$ and $FF_{1-71}$, $\Delta\varpi_{spec}$, versus chemical shift differences between intermediate and native states (of $FF_{1-71}$), $\Delta\varpi_{disp}$, extracted from relaxation dispersion data. RMSD values between data sets calculated excluding points marked by residue numbers are shown in the top left corner of each plot. Resonance assignments for $^{15}N$,$^{13}C$-labeled $FF_{1-60}$ were obtained with the use of standard triple-resonance NMR experiments (*43*, *44*).

## References and Notes


1. D. J. Brockwell, S. E. Radford, *Curr. Opin. Struct. Biol.* **17**, 30 (2007).
2. V. Daggett, A. Fersht, *Nat. Rev. Mol. Cell Biol.* **4**, 497 (2003).
3. C. M. Dobson, A. Sali, M. Karplus, *Angew. Chem. Int. Ed.* **37**, 868 (1998).
4. A. P. Capaldi, C. Kleanthous, S. E. Radford, *Nat. Struct. Biol.* **9**, 209 (2002).
5. D. M. Korzhnev *et al.*, *Nature* **430**, 586 (2004).
6. T. L. Religa, J. S. Markson, U. Mayor, S. M. V. Freund, A. R. Fersht, *Nature* **437**, 1053 (2005).
7. S. Auer *et al.*, *Phys. Rev. Lett.* **99**, 178104 (2007).
8. D. M. Korzhnev, L. E. Kay, *Acc. Chem. Res.* **41**, 442 (2008).
9. A. J. Baldwin, L. E. Kay, *Nat. Chem. Biol.* **5**, 808 (2009).
10. A. G. Palmer III, C. D. Kroenke, J. P. Loria, *Methods Enzymol.* **339**, 204 (2001).
11. D. F. Hansen, P. Vallurupalli, P. Lundström, P. Neudecker, L. E. Kay, *J. Am. Chem. Soc.* **130**, 2667 (2008).
12. P. Vallurupalli, D. F. Hansen, E. Stollar, E. Meirovitch, L. E. Kay, *Proc. Natl. Acad. Sci. U.S.A.* **104**, 18473 (2007).
13. T. I. Igumenova, U. Brath, M. Akke, A. G. Palmer III, *J. Am. Chem. Soc.* **129**, 13396 (2007).
14. D. M. Korzhnev, T. L. Religa, P. Lundström, A. R. Fersht, L. E. Kay, *J. Mol. Biol.* **372**, 497 (2007).
15. P. Neudecker, A. Zarrine-Afsar, A. R. Davidson, L. E. Kay, *Proc. Natl. Acad. Sci. U.S.A.* **104**, 15717 (2007).
16. P. Vallurupalli, D. F. Hansen, L. E. Kay, *Proc. Natl. Acad. Sci. U.S.A.* **105**, 11766 (2008).

17. A. Cavalli, X. Salvatella, C. M. Dobson, M. Vendruscolo, *Proc. Natl. Acad. Sci. U.S.A.* **104**, 9615 (2007).
18. Y. Shen *et al.*, *Proc. Natl. Acad. Sci. U.S.A.* **105**, 4685 (2008).
19. D. S. Wishart *et al.*, *Nucleic Acids Res.* **36** (Web server issue), W496 (2008).
20. M. Allen, A. Friedler, O. Schon, M. Bycroft, *J. Mol. Biol.* **323**, 411 (2002).
21. P. Jemth *et al.*, *Proc. Natl. Acad. Sci. U.S.A.* **101**, 6450 (2004).
22. P. Jemth *et al.*, *J. Mol. Biol.* **350**, 363 (2005).
23. P. Jemth, C. M. Johnson, S. Gianni, A. R. Fersht, *Protein Eng. Des. Sel.* **21**, 207 (2008).
24. A. Matouschek, J. T. Kellis Jr., L. Serrano, A. R. Fersht, *Nature* **340**, 122 (1989).
25. J. P. Loria, M. Rance, A. G. Palmer III, *J. Am. Chem. Soc.* **121**, 2331 (1999).
26. D. F. Hansen, P. Vallurupalli, L. E. Kay, *J. Phys. Chem. B* **112**, 5898 (2008).
27. R. Ishima, D. A. Torchia, *J. Biomol. NMR* **25**, 243 (2003).
28. R. Ishima, J. Baber, J. M. Louis, D. A. Torchia, *J. Biomol. NMR* **29**, 187 (2004).
29. P. Lundström, D. F. Hansen, P. Vallurupalli, L. E. Kay, *J. Am. Chem. Soc.* **131**, 1915 (2009).
30. P. Lundström, D. F. Hansen, L. E. Kay, *J. Biomol. NMR* **42**, 35 (2008).
31. Single-letter abbreviations for the amino acid residues are as follows: A, Ala; C, Cys; D, Asp; E, Glu; F, Phe; G, Gly; H, His; I, Ile; K, Lys; L, Leu; M, Met; N, Asn; P, Pro; Q, Gln; R, Arg; S, Ser; T, Thr; V, Val; W, Trp; and Y, Tyr.
32. Materials and methods are available as supporting material on *Science* Online.
33. N. R. Skrynnikov, F. W. Dahlquist, L. E. Kay, *J. Am. Chem. Soc.* **124**, 12352 (2002).
34. N. Tjandra, A. Bax, *Science* **278**, 1111 (1997).
35. D. S. Wishart, D. A. Case, *Methods Enzymol.* **338**, 3 (2001).
36. M. V. Berjanskii, D. S. Wishart, *J. Am. Chem. Soc.* **127**, 14970 (2005).
37. Y. Shen, F. Delaglio, G. Cornilescu, A. Bax, *J. Biomol. NMR* **44**, 213 (2009).
38. S. Raman *et al.*, *Science* **327**, 1014 (2010); published online 4 February 2010 (10.1126/science.1183649).
39. R. Das, D. Baker, *Annu. Rev. Biochem.* **77**, 363 (2008).
40. M. Rückert, G. Otting, *J. Am. Chem. Soc.* **122**, 7793 (2000).
41. A. Fersht, *Structure and Mechanism in Protein Science: A Guide to Enzyme Catalysis and Protein Folding* (W. H. Freeman, New York, 1999).
42. T. L. Religa *et al.*, *Proc. Natl. Acad. Sci. U.S.A.* **104**, 9272 (2007).
43. A. Bax, *Curr. Opin. Struct. Biol.* **4**, 738 (1994).
44. M. Sattler, J. Schleucher, C. Griesinger, *Prog. Nucl. Magn. Reson. Spectrosc.* **34**, 93 (1999).
45. H. Q. Feng, Z. Zhou, Y. W. Bai, *Proc. Natl. Acad. Sci. U.S.A.* **102**, 5026 (2005).
46. B. G. Wensley *et al.*, *Nature* **463**, 685 (2010).
47. M. E. McCully, D. A. C. Beck, A. R. Fersht, V. Daggett, *Biophys. J.* **99**, 1 (2010).
48. S. W. Englander, L. Mayne, M. M. G. Krishna, *Q. Rev. Biophys.* **40**, 287 (2007).
49. P. Lundström *et al.*, *J. Biomol. NMR* **38**, 199 (2007).
50. V. Y. Orekhov, D. M. Korzhnev, L. E. Kay, *J. Am. Chem. Soc.* **126**, 1886 (2004).
51. Y. Shen, A. Bax, *J. Biomol. NMR* **38**, 289 (2007).
52. We thank J. Forman-Kay (Hospital for Sick Children, Toronto) for providing laboratory space and useful discussions, P. Jemth (Uppsala Univ.) for providing plasmids for protein expression, R. Vernon (Univ. of Washington, Seattle) for valuable discussions, and R. Muhandiram (Univ. of Toronto) for NMR support. T.L.R. acknowledges the European Molecular Biology Organization (ALTF 827-2006) and the Canadian Institutes of Health Research (CIHR) for postdoctoral fellowships. L.E.K. holds a Canada Research Chair in Biochemistry. This work was supported by a grant from the CIHR to L.E.K. The structural ensembles of the WT FF domain–folding intermediate have been deposited in the Protein Data Bank (PDB; www.rcsb.org) with accession code 2KZG.

**Supporting Online Material**

www.sciencemag.org/cgi/content/full/329/5997/1312/DC1
Materials and Methods
Figs. S1 and S2
Tables S1 to S4
References

3 May 2010; accepted 24 June 2010
10.1126/science.1191723

REPORTS

# Electromechanical Computing at 500°C with Silicon Carbide

**Te-Hao Lee,[1]* Swarup Bhunia,[2]* Mehran Mehregany[2]***

**Logic circuits capable of operating at high temperatures can alleviate expensive heat-sinking and thermal-management requirements of modern electronics and are enabling for advanced propulsion systems. Replacing existing complementary metal-oxide semiconductor field-effect transistors with silicon carbide (SiC) nanoelectromechanical system (NEMS) switches is a promising approach for low-power, high-performance logic operation at temperatures higher than 300°C, beyond the capability of conventional silicon technology. These switches are capable of achieving virtually zero off-state current, microwave operating frequencies, radiation hardness, and nanoscale dimensions. Here, we report a microfabricated electromechanical inverter with SiC complementary NEMS switches capable of operating at 500°C with ultralow leakage current.**

High-temperature measurement and control instrumentation require microcontrollers, in addition to sensors and interface electronics, for a variety of important applications (such as automotive and aerospace propulsion systems, deep-well drilling, and geothermal exploration) in which the ambient temperature typically ranges from 300° to 600°C (*1*). However, limited by their band gaps, the mature silicon technologies [for example, a complementary metal-oxide semiconductor (CMOS)] are not applicable to this field due to excessive leakage caused by p-n junction degradation and thermoionic leakage (*2*). At these temperatures, thermally excited electrons in silicon can overcome the gate potential, and the intrinsic carriers excited by the thermal energy exceeds the amount of doped carriers. Thus, the electrical properties will be considerably influenced by thermally generated carriers, and the devices fail. To this end, wide–band-gap semiconductors like SiC have been of interest for these applications. Such materials, with adequate conductivity, offer a potential solution to expensive thermal-management and heat-sinking requirements, which pose a major barrier to continued shrinking of electronics. To date, the SiC electronic platform has been regarded as the most viable technology for high-temperature applications. Various field-effect transistor (FET) architectures have been considered as building blocks of this platform. Among alternative device architectures, the SiC junction field-effect transistor (JFET) is the most promising candidate for high-temperature logic applications (*3*, *4*). Lack of good-quality gate insulator and low inversion-layer mobility have limited the development of SiC metal-oxide semiconductor FETs (*5*–*7*). On the other hand, Shottky-based metal semiconductor FETs exhibit notable gate-to-channel leakage at elevated temperatures (*8*). As a depletion-mode device, the JFET

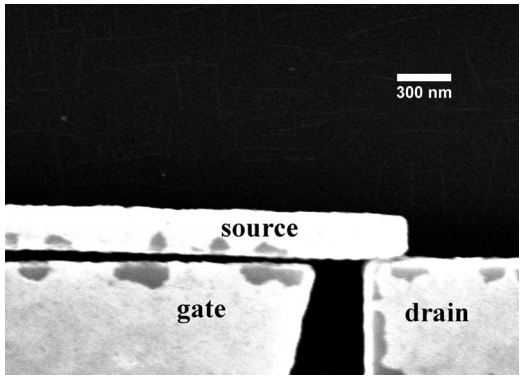


**Fig. 1.** A scanning electron micrograph showing the ON state of the three-terminal SiC NEMS switch. The spacing between the gate and drain is 300 nm. The initial actuation-gap height, defined as the distance between source and gate, is 150 nm without applying any potential. Lateral movement of the cantilever due to electrostatic attraction between the source and gate causes the beam to contact the drain. After the contact of source and drain, the gap between source and gate becomes only 25 nm.

[1]Department of Materials Science and Engineering, Case Western Reserve University, Cleveland, OH 44106, USA. [2]Department of Electrical Engineering and Computer Science, Case Western Reserve University, Cleveland, OH 44106, USA.

*To whom correspondence should be addressed. E-mail: tehao@case.edu (T.-H.L.); swarup.bhunia@case.edu (S.B.); mehran@case.edu (M.M.)

# A Transient and Low-Populated Protein-Folding Intermediate at Atomic Resolution

Dmitry M. Korzhnev, Tomasz L. Religa, Wiktor Banachewicz, Alan R. Fersht, and Lewis E. Kay

*Science*, 329 (5997), • DOI: 10.1126/science.1191723

**Transient Protein Conformations**

Transient conformations are important to protein function; however, detecting and characterizing these states is technically challenging. Korzhnev *et al.* (p. 1312; see the Perspective by Al-Hashimi) combined recently developed methods to determine the three-dimensional atomic-resolution structure of a transient intermediate of a four-helix bundle protein domain. The intermediate formed rapidly but, owing to structural peculiarities, slowly rearranged into its native state. The methods can be applied not only to folding intermediates but also to excited states important for protein function.